

# Investigation of Deep Learning for Real-Time Melt Pool Classification in Additive Manufacturing

Zhuo Yang, Yan Lu, Ho Yeung, Sundar Krishnamurty

**Abstract**— Consistent melt pool geometry is an indicator of a stable laser powder bed fusion (L-PBF) additive manufacturing process. Melt pool size and shape reflect the impact of process parameters and scanning path on the interaction between the laser and the powder material, the phase change and the flow dynamics of the material during the process. Current L-PBF processes are operated based on predetermined toolpaths and processing parameters and consequently lack the ability to make reactions to unexpected melt pool changes. This paper investigated how melt pool can be characterized in real-time for feedback control. A deep learning-based melt pool classification method is developed to analyze melt pool size both fast and accurately. The classifier, based on a convolutional neural network, was trained with 2763 melt pool images captured from a laser melting powder fusion build using a serpentine scan strategy. The model is validated through 2926 new images collected from a different part in the same build using ‘island’ serpentine strategy with predictive accuracy of 91%. Compared to a traditional image analysis method, the processing time of the validation images is reduced by 90 %, from 9.72 s to 0.99 s, which gives the feedback control a reaction time window of 0.34 ms/image. Results show the feasibility of the proposed method for a real-time closed loop control of L-PBF process.

## I. INTRODUCTION

Additive manufacturing (AM), as opposed to the subtractive manufacturing technology, is defined as a process of joining material to make parts directly from 3D models [1]. As one of layerwise AM techniques, laser powder bed fusion (L-PBF) uses a laser source to scan and fuse a cross-sectional area of thin spread metal powder [2]. During the repeating and layer-by-layer process, loose metal powder is transformed to dense AM parts. AM part undergoes three major subprocesses to complete the powder-bulk material transformation: heat absorption, melt pool formation, and solidification [3]. The three subprocesses occur sequentially. Melt pool formation is the intermediate process that bridges the other two. Melt pool evolution involves the physics of material phase change, thermal conduction, fluid dynamics, and some other physical phenomena that could occur during this process.

Melt pool geometry is a measurable process characteristic which reflects the process stability and is correlated to the final material properties. Recent studies indicate microstructure and mechanical properties of AM-produced parts are significantly influenced by the size and shape of melt pool [4]. It is also widely accepted that the porosity in L-PBF parts can be

attributed to improper melt pool formation due to lack of fusion or trapped gas [5], [6]. Melt pool width and hatch distance determine the overlapping conditions between adjacent tracks, where overlapping conditions can affect the microstructure of AM part [7]. A feasible way to improve AM part quality is through melt pool size control and melt pool variation reduction, which could be achieved by manipulating processing parameters such as laser power, beam size and scanning speed.

Various factors were analyzed and many of them were found to affect melt pool formation. For example, energy density is believed to have strong impact on melt pool size. Experiments and simulations revealed that higher energy input produces a larger melt pool when other conditions remain the same [8]-[11]. So a typical method to control the melt pool size during an L-PBF process is to modify the energy input. However, open loop melt pool control cannot compensate the effects from other factors which are not controllable or difficult to control. Melt pool on a straight track, though operated using a constant laser power and constant scan speed, can vary due to the variation of part geometry or environmental conditions [12]. For example, overhanging area and non-overhanging area melt pool can have 20% size difference for the same energy intensity input [8]. The scan pattern is another factor which could cause the melt pool to change irregularly [13]. The melt pool size during a L-PBF process can vary from time to time, either too large or too small compared to expected values. If not detected and corrected, the melt pool anomalies may lead to poor material properties or part failures. In-situ melt pool measurement and real-time melt pool control have the great potential to reduce the waste from part scraps and improve part quality. The in-situ monitoring procedure can provide the melt pool information to the AM machine in real time, and the second procedure run analysis to modify process parameters and/or scan strategy.

In-situ monitoring in L-PBF systems can detect and localize the onset of defects during the manufacturing process [14]. Typical in-situ monitoring methods include surface optical or thermal imaging, melt pool size measurement [15], [16], melt pool dynamic monitoring [17], heat movement tracking [18], etc. For example, the balling phenomenon that caused by low energy input [19] is one of the significant factors that impair AM part quality [20]. The defect is visually detectable through melt pool images [20]. These types of in-situ images capture local melt pool information during manufacturing, which can be difficult to access once the current layer is covered by a new layer of powder.

\*Research supported by NIST.

Zhuo Yang and Sundar Krishnamurty are with University of Massachusetts Amherst, Amherst, MA 01003 USA

Yan Lu and Ho Yeung are with the National Institute of Standards and Technology, Gaithersburg MD 20899 USA. (e-mail: yan.lu@nist.gov)

A high-speed camera used for L-PBF melt pool monitoring can capture more than 10000 frames every second [21]. It not only suggests that thousands of images could be generated for one layer, but also indicates a need of developing a fast image processing method to characterize melt pool geometry. Computer vision algorithm is used to classify anomalies at the powder spreading stage [22] and for powder characterization [23]. Machine learning is also widely used in AM for classifying defects and predicting fusion quality, [24], [25], which can provide an instant solution.

Although numerous research efforts have been reported on monitoring and control of AM processes to improve part quality, most of the research objective of melt pool monitoring is to collect in-situ monitoring data to validate physics-based simulation models [26]-[30]. There are still gaps for real-time closed loop control of L-PBF processes [31]. The barrier lies in the processing time needed for raw data analysis or the high computation load of making prediction out of simulation models. Data-driven modeling techniques capable of processing large volumes of streaming data are strongly recommended for real-time control [31].

This paper investigates real-time melt pool monitoring and classification methods for L-PBF processes, aiming to examine their applicability in real-time process control. The study focuses on investigating the fundamental anomaly detection of in-situ AM process in time, accuracy, and robustness perspective. This study has resulted in a classification method that can characterize four types of melt pool sizes: none, small, regular, and large. A total of 5689 in-situ melt pool images are collected to build and validate the proposed classification model. The classifier, a convolutional neural network (CNN), is trained and tested with images captured from two L-PBF built parts using different scan strategies. Section II introduces the experimental build setup. The details of the data collected during the build and analysis of the image data is presented in Section III. Section IV and Section V present model validation results and discussions.

## II. EXPERIMENTAL SETUP

An experimental L-PBF build was conducted on the Additive Manufacturing Metrology Testbed (AMMT) at National Institute of Standards and Technology (NIST) [32]. The AMMT is a fully customized metrology instrument that enables flexible control and measurement of the L-PBF process. Figure 1 shows the schematic of the AMMT system. Two cameras were installed for process monitoring, including a high resolution camera that captures the layerwise images of the entire part, and a high-speed camera used to capture melt pool images. The Galvo mirror system and the beam splitter allow the high-speed camera to focus on current laser melting spot. Emitted light from the melt pool, through a 850 nm bandpass filter (40 nm bandwidth), is imaged on the camera sensor. On AMMT both Galvo and laser command are updated on field programmable gate array (FPGA) at 100 KHz.

An in-house developed AM software named SAM, which is capable of stereolithography (STL) slicing, scan path planning, G-code generation and interpretation [21], was used to program the different scan strategies for the experiment. Inconel 625 powder and build plate were used. the substrate

has a dimension of 102 mm x 102 mm x 13 mm. Twelve rectangular parts (with chamfered corners) of dimensions 10 mm x 10 mm x 5 mm were laid on the substrate, with a minimum spacing of 10 mm between parts. Each part was built with a different scan strategy [21]. In this study, images used for training and testing purposes are collected from two different parts using a serpentine strategy and an “island” serpentine strategy respectively. The melt pool was monitored by the high-speed camera which is optically aligned with the heating laser, such that the image of the melt pool is maintained stationary within the camera’s field of view. The camera was triggered at every 500  $\mu$ s (i.e., 2000 frames per second), with an integration time of 20  $\mu$ s.

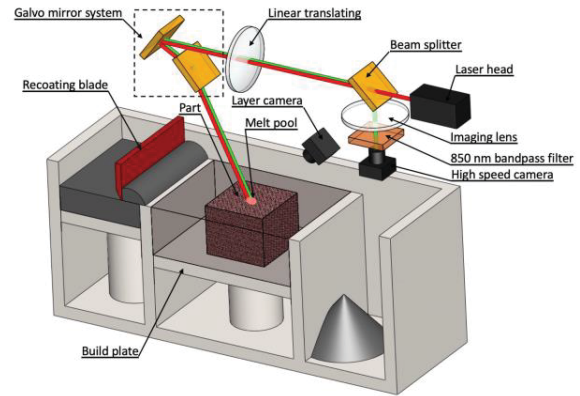


Figure 1. Schematic of AMMT system

## III. METHOD AND IMAGE DATA ANALYSIS

In this study, images collected from the AMMT build are used to demonstrate and validate the proposed melt pool classification method. Total 2763 melt pool images were captured from the part with a serpentine scan strategy which are used as training data. Another 2926 images captured from the “island” serpentine scan strategy part are used to evaluate the classification accuracy. Both image sets include images from the same layer. This section presents the melt pool image preprocessing and classification methods. The details of the training data and the test data are discussed at the end.

### A. Image preprocessing

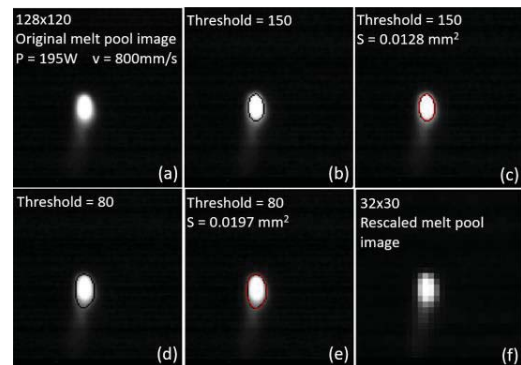


Figure 2. Melt pool image preprocessing. (a) an original grayscaled melt pool image. (b) and (d) melt pool boundaries detected based on two different threshold values. (c) and (e) approximated melt pool shapes using least square ellipse fitting. (f) a resized image.

### 1) Melt pool measurement

Figure 2(a) is an original melt pool image taken from the high-speed camera for one focal point. The grayscale of the image is from 0 to 255. A higher melt pool intensity correlates to a larger grayscale value, which corresponds to a brighter pixel in the image. The boundary of a melt pool, which highlights the melt pool phase change frontier, is detected by a defined threshold value. Figure 2(b) and (d) show the boundaries detected based on threshold grayscale values 150 and 80, respectively. They represent two actual melt pool edges. Lower threshold values usually result in larger melt pool sizes. In this study, the threshold value is set to 150 since the outline is closer to a manual sketched melt pool boundary.

Usually, the melt pools created by a moving laser beam present irregular shapes, which can be visually observed from both simulations and experiments [33], [34]. This irregularity raises the difficulty of measuring melt pool width and length. To address the problem, this study first approximates each melt pool boundary with a regular ellipse shape using least square fitting [35]. With that, the melt pool sizes can be measured uniformly. The fitted ellipse outlines are marked in red color as shown in Figure 2(c) and (e). To address this issue, each melt pool is approximated by a regularly shaped ellipse (c and e). As a result, melt pool length and width can be calculated uniformly for all images. More specifically, melt pool width is defined as twice of the minor radius and melt pool length is equal to twice of the major radius. The final melt pool area, instead of calculated by counting pixels above the threshold, is defined as the area of the approximated ellipse.

In Figure 2, the area of approximated ellipse is  $0.0128 \text{ mm}^2$  based on the outline detected by threshold grayscale value 150. However, a lower threshold value 80 results in the ellipse expanded to  $0.0197 \text{ mm}^2$ .

### 2) Image labeling

The objective of this work is to detect irregular melt pool formation and investigate the use of real-time control in L-PBF system. When a melt pool area exceeds or measures much less than the expected value, the AM machine should be informed. During an AM process, melt pool size is expected to vary within a range to maintain appropriate overlapping conditions. If a melt pool is too small to connect to adjacent melt pools, the unmelted powder in between may develop to pores. On the other hand, oversized melt pools may lead to overheating and re-melting issues. Without losing generality, based on the average hatch distance of this study, the normal range of the melt pool area based on the threshold value 150 is defined as from  $0.011 \text{ mm}^2$  to  $0.014 \text{ mm}^2$ .

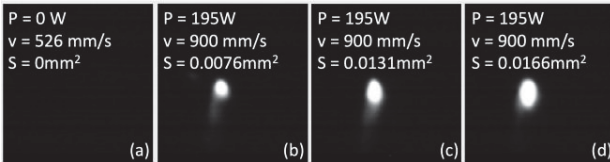


Figure 3. Four typical melt pool images are labeled differently

Melt pools are labeled into four categories: no melt pool observed (Z), smaller melt pool (S), normal melt pool (N), and larger melt pool (L). shows an example of melt pool labels. All images are captured under the same laser power and scan speed. According to the measured melt pool area, (a) through

(d) are labeled as “Z”, “S”, “N”, and “L” respectively. The details of the processing parameters and measurement are provided on the figures.

Images that labeled into the same class can have different characteristics. From the imaging perspective, they may have a different width, length, deflection angles, tails, and outline. As shown in Figure 4, all four melt pool images are produced by the same processing parameters. However, they have different characteristics which may be caused by beam location, moving direction, and other random factors. They are all labeled as “N” based on the labeling criteria,  $0.011$  to  $0.014 \text{ mm}^2$ . However, the images look very different according to the melt pool shape, tail, and orientation. Classify different images into the correct melt pool category is the primary goal of the classifier.

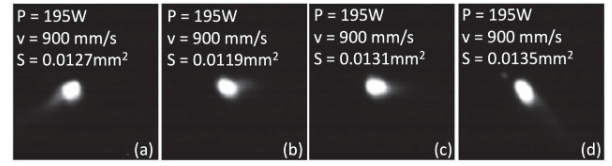


Figure 4. Melt pool that labeled to “N” may have distinguished characteristics

### 3) Resizing

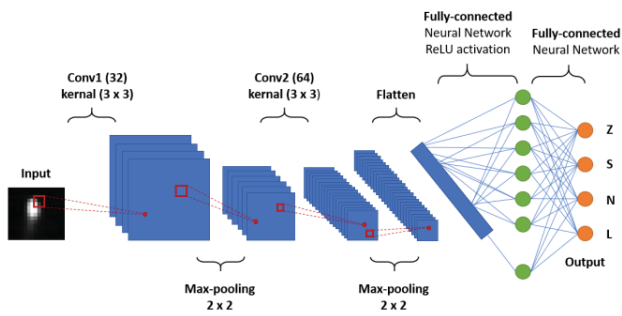
The raw image, which is  $128 \times 120$  pixels, is down-sampled to  $32 \times 30$  pixels for higher computational efficiency. From the modeling perspective, the input dimension can be reduced from 15360 (original) to 960 (resized). Meanwhile, down-sampling can reduce file sizes and potentially improve storage efficiency. In this experiment, the part using the serpentine strategy contains 250 layers with 2763 images generated at each layer. If all the images are stored, it requires about 10.53 GB of space. After the resizing, the storage need is 1.29 GB with an 87 % reduction. Figure 2(f) shows an example of a resized melt pool image.

### B. Melt pool classification

Convolutional Neural Network (CNN) is a multi-layer feedforward artificial neural network which is firstly proposed for two-dimensional image processing [36]. A typical CNN architecture includes nested convolutional and pooling layers followed by fully connected layers at the end. The input of CNN in this study is the 1-channel image matrices containing the intensity values at each position. Conv is the convolutional layers apply a set of filters that each of which is connected to a small region of the output of the last layer, the receptive field [37].

Figure 5 shows the CNN architecture for melt pool classification. This Sequential typed CNN model includes 2 Conv2D layers. The first layer contains 32 nodes with  $3 \times 3$  filter matrix. The second layer contains 64 nodes by the same kernel size. Rectified linear units (ReLU) is the activation function used in the model. It adds non-linear transformations to the output response of the convolutional or fully connected layers [37]. The pooling layer performs a form of non-linear down-sampling along both spatial dimensions, leading to a reduced spatial size of the output. The maximum pooling size is set to  $2 \times 2$ . The outputs of the model are ‘Z’, ‘S’, ‘N’, and ‘L’, which labels the melt pool size to non, small, normal, and large.





C. Figure 5. CNN architecture for melt pool classification

#### 1) Training data

Training data is constructed with the 2763 images collected from the part using a serpentine scan strategy. The conceptual toolpath of the serpentine strategy is shown in Figure 6(a). Laser beam starts from the bottom right and ends at the upper left corner. When laser beam is moving in the inner area, the laser power and the scan speed are set to  $P=195\text{W}$  and  $v=800\text{ mm/s}$  respectively. The laser is turned off at the end of each straight track. The turning strategy is designed to avoid overheating since the laser scan has a reduced speed near the edge when preparing to change direction. A pre-contour scan and a post-contour scan with lower laser power are added at the beginning and end of each layer to create edges. The beam diameter remains constant through the entire experiment. Using a simplified form  $P/v$  to represent energy intensity, Figure 6(b) indicates the same energy density for the inner area powder fusion. Ideally, according to the previous study [8], melt pool size should be measured around a mean value with small variations.

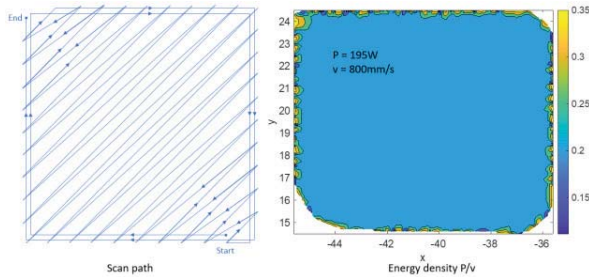


Figure 6. Serpentine scan strategy for the training images. (a) The conceptual toolpath and (b) A simplified energy density map.

However, the image analysis results shown in Figure 6 reveal that the melt pool size measured has substantial variations. The contour plot is created from the melt pool area characterization, and the dots show the irregular melt pool type distribution classified based on the threshold values of a normal melt pool size. Red and blue points represent “L” and “S” types melt pool, respectively. Most of the inner area has regular sized melt pools. Melt pools located near the edge are seen smaller than the expected value, which may be caused by insufficient energy input. At the upper left corner, a larger melt pool appeared which might be caused by residual heat.

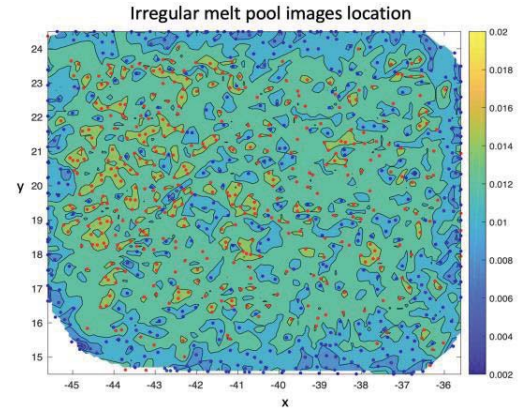


Figure 7. Training data melt pool area color map and irregular melt pool distribution

Figure 8 is a histogram that shows the frequency for different melt pool type. There are 370 “Z”, 446 “S”, 1450 “N”, 407 “L” typed melt pool images in the training data set. The average effective melt pool (“S”, “N”, and “L”) area is  $0.0124 \pm 0.0018\text{ mm}^2$ .

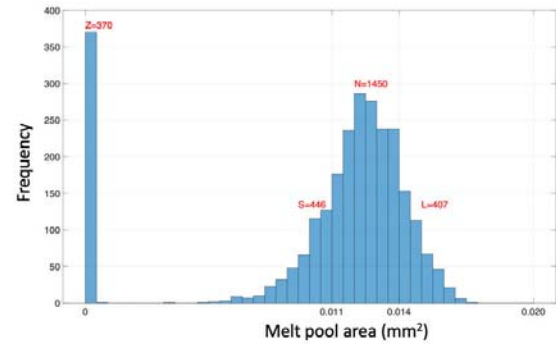


Figure 8. Histogram of the training data

#### 2) Testing data

Images used to test the classifier are collected from a different part using an “island” serpentine scan strategy. Figure 9 shows the scan strategy concept and a simplified energy density color map. The scanning path is divided into four “islands”. The laser beam scans each “island” using serpentine patterns. Similarly, the laser was turned off during scan direction changes near the edges of each “island”. Laser beam starts from the lower right and ends at the upper left. For the inner areas, the laser power and scan speed are set to 195W and 800 mm/s, which are the same as the training data.

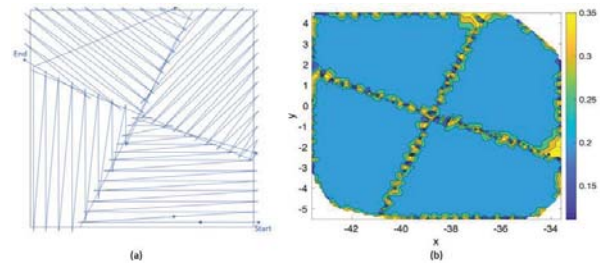


Figure 9. (a) Island serpentine scan strategy for the test image set, and (b) A simplified energy density map

#### IV. RESULTS

There are total 2926 images used to validate the melt pool classification model. The overall accuracy is 90.84 % with 268 incorrect classifications. Figure 10 shows the contour plot of the actual melt pool area and the irregular melt pool positions classified using the CNN model. Red and blue points mark the locations of “L” and “S” types of melt pool. From the actual measurement, melt pools on the edges and the upper left “island” tend to be smaller than expected based on the input energy intensity. Most of the oversized melt pools are found on the upper right “island”. Visually, most of the CNN classified melt pools are located at the correct positions.

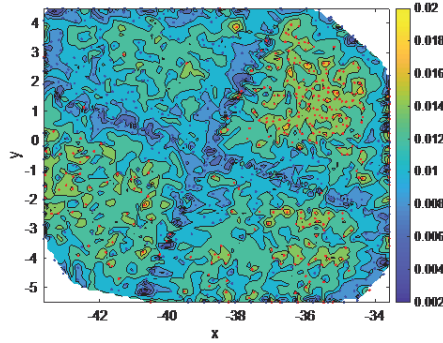


Figure 10. Actual melt pool area map of the test data and the CNN classified irregular melt pool

Melt pool heat maps are shown in Figure 11 to compare the differences between the actual and the CNN classified melt pool distributions. The heat map graphically represents the melt pool types on the entire layer. In the actual measurement map (Figure 10 (a)), “S” (blue) type melt pools are frequently observed on the “island” edges. Normal size melt pools, “N” (green), still dominate most of the area. However, the melt pools at the center of the upper right “island” tend to be oversized, “L” (yellow). The CNN classified melt pool type heat map generally matches the actual result. Some “L” type melt pools are missing and replaced by “N” type (Figure 10 (b)), which indicates that the classifier may have lower performance on this type of images.

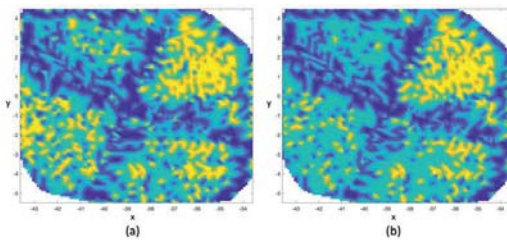


Figure 11 (a) Heat map of the actual melt pool type (b) Heat map of the CNN classified melt pool type. Blue: “S”. Green: “N”, Yellow: “L”.

Figure 12 reveals the classification results of the test images using the CNN classifier. As shown in (a), the classification model performs the best for the “S” category. 4.93 % (22) of “S” images are incorrectly classified. For “N” images, although there are total 105 incorrect classification results, error ratio is under 8 % since this category has most images. “L” images exhibit the largest classification error rate, 36.64% being misclassified. Figure 11 (b), (c) and (d) show

the details of those wrongly classified melt pool from type to type. (b) reveals that all the wrongly classified “S” type images are classified as the “N” type by the CNN model. In (c), the “N” type images, if misclassified, can be either assigned to “S” (79.2 %) or assigned to “L” (20.8 %). (d) shows that 100% of misclassified 141 “L” images are wrongly assigned to “N” group. “Z” images are all correctly classified.

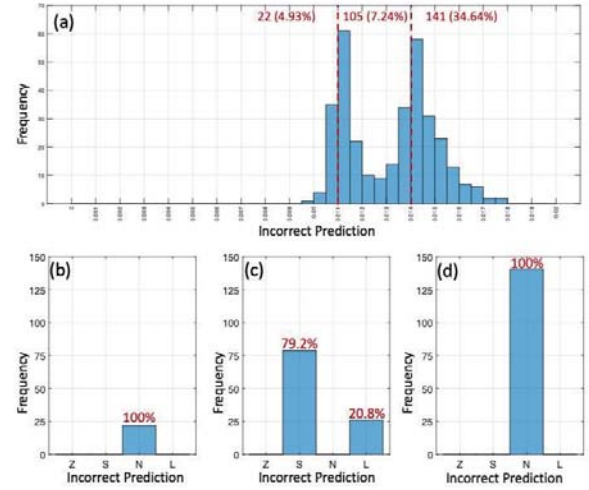
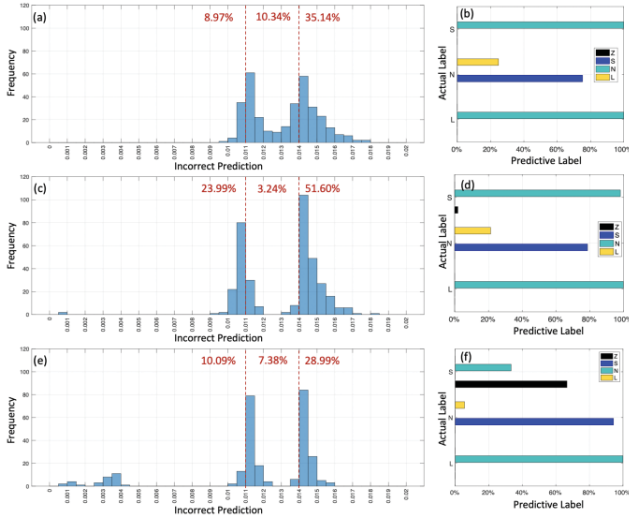


Figure 12. (a) Incorrect classification rate for all types of the images. (b) Type “S” misclassified images (c) Type “N” misclassified images (d) Type “L” misclassified images

#### V. DISCUSSION

The major objective of this work is to investigate a applicable melt pool image classification method that can quickly provide accurate information for real-time L-PBF closed loop control. To date, commercial AM machines uses fixed scan strategy throughout the AM building process. The laser beam would follow the pre-determined tool path and processing parameters such as laser power and scan speed to build part unless receiving mandatory external operation. However, such subject-specific features of AM parts as geometry and other stochastic error may accumulate during the building process. AM real-time control can potentially reduce the risk of AM part failure if the machine can make appropriate response based on in-situ monitoring information. According to this need, this study selects the essential in-situ melt pool feature, melt pool size, to approve the concept of AM in-situ monitoring. Other readable features such as spattering are main topics for future work.

The CNN based classification model is built based on 2763 images collected from the NIST AMMT tester. The model is validated using a test data set of 2926 images, with a 90.84 % classification accuracy. The CNN approach though cannot as accurate as ellipse approximation method, it provides the AM fast reaction time considering the high scanning speed. Incorrect classifications are mainly located around the boundary values of the regular melt pool size. Both “S” and “N” melt pool types can be well recognized by the model with classification errors of 4.93 % and 7.24 %. The model seems less sensitive to type “L” melt pools and performs worst with a 34.64 % error rate, which may because of the relatively smaller sample size of this type of images.



frequency of misclassification of the 64x60, 16x15, and 8x8 CNN models, respectively. (b), (d) and (f) The details of the misclassification for each model. Y axis represents the original label of each image. The bar represents incorrect predicted labels. Blue: “Z”. Orange: “S”. Yellow: “N”. Purple: “L”.

Computational speed is the biggest concern for the real-time control system. The traditional method can provide accurate melt pool measurement but lacks processing efficiency. Using the same computer, the processing time of the traditional method to measure and classify 2926 images takes 9.72 s. It allocates about 3.4 ms to each image analysis. This represents a significant spatial delay, for example for the 800 mm/s scanning speed of this study, of 3 mm location offset between the melt pool measured and the current scanning location. Considering that the sample parts have a 10×10 mm<sup>2</sup> cross-sectional area, the real-time control becomes impossible. However, the computation time reduce to 0.3370 ms (90 % reduction) based on the same computer with the CNN classifier used. The shorter time delay provides the AM machine a capability modification window within 0.25mm based on the 800 mm/s laser scanning speed. As shown in Figure 10, Both the “S” and “L” type melt pools are highly clustered. The real-time control implementation can make immediate response once detecting irregular melt pools. Mediation can be taken to decrease the failure probability of the build.

Table 1 lists the training and real-time processing time and the corresponding classification accuracy for different image down-sample strategies. The purpose of down-sampling is to check the performance and influence of image resolution. The processing speed can be significantly reduced by hardware such as FPGA or GPU. However, this work does not use GPU for model training since it aims to organically investigate the minimum requirement of melt pool image resolution. This information can help to modify the tradeoff between image quality and frequency for the camera equipment. The highest resolution does not necessarily bring more accuracy to the model. However, its processing time approaches the traditional method. The table also reveals the CNN based classification method can still perform well for 8×8 images. In this situation, each classification only takes 0.05 ms, which

increases the closed loop bandwidth further for the real-time feedback control. Although it seems reasonable to do deeper down-sampling, further tests are required to validate the statement.

Table 1. Computational time estimated and classification accuracy for different down-sampling strategies

Size	Training time (s)	Total processing time per image (s)	Predictive accuracy
64x60	602.03	7.18 (0.00245)	88.62 %
32x30	94.69	0.99 (0.00034)	90.84 %
16x15	27.28	0.35 (0.00012)	89.47 %
8x8	9.14	0.15 (0.00005)	90.77 %

Figure 13 illustrates the detailed classification results for the down-sampling scenarios in Table 1. (a) and (c) show the histogram of incorrect classification frequency of different melt pool types for the 64×60 and 16×15 image sets, respectively. 64×60 resized model is more sensitive to “L” type images but less sensitive to “S” and “N” type images. As shown in Figure 13(b), both incorrect “S” and “L” images are misclassified as “N”. The model trained with 16×15 images has good performance for regular melt pool but is less sensitive to irregular melt pool images. Figure 13(d) shows that the model has classified some images with very small melt pool to “Z”. The model from the 8×8 image set has a similar overall classification accuracy but Figure 13(f) indicates the model can easily classify the small melt pool into “Z”. The error may increase the difficulty of real-time control.

Melt pools with sizes close to the boundary (0.011 and 0.014) have a higher chance to be classified incorrectly. Different factors may cause this issue. For example, the labeling procedure can cause this issue. The melt pool area is originally calculated from its approximating ellipse. For irregular shapes, the least square fitting may encounter difficulties when computing matrix inversion. Hence it is possible that the original images were assigned with wrong labels. The initial uncertainty of L-PBF process may also cause variation in the AM images [38], [39]. Further investigation for the images and the deep learning techniques are required to improve classification accuracy. This CNN based model can be utilized for both real-time feedback and feedforward control. If the goal is to maintain a consistent melt-pool, the real-time classification results can be used as feedback signal to adjust the instantaneous laser power. Laser response time is usually in the order of 10 to 20 μs. On AMMT both Galvo and laser commands are updated on FPGA at 100 kHz, and the laser power scaling should be comfortably completed within one clock cycle; assuming the 16 x 15 size is adapted, the total delay should be around 150 μs or 120 μs at 0.8 m/s scan speed. This is approximately one melt-pool length only. For forward control, the images from current layer can be used to train the model on real-time and scale the laser power for the next layer based on the model output. Since powder spreading itself would take 15 s, it is possible that with a smaller image size and improvement in hardware, all the computation can be completed before the new layer scan starts. Future works would focus on implement this highly efficient melt pool classification method into L-PBF real-time control system.



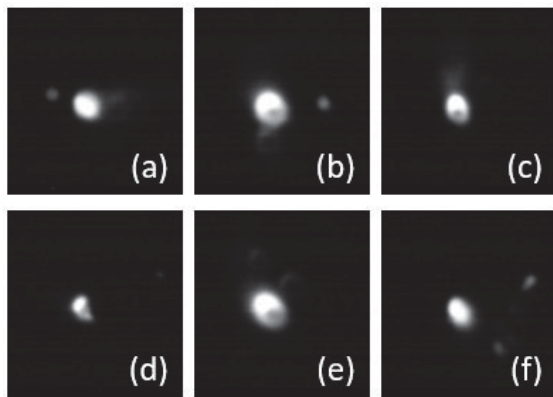


Figure 15. Irregular melt pool images

Current work has verified the concept of AM real-time control and applicability in AM testbed. Machine learning can provide faster processing speed to detect the anomaly in melt pool formation than the traditional method. In fact, the traditional method by counting the pixels may provide the most accurate classification with longer processing time. Machine learning has been widely used in AM for prediction, optimization, and classification [40], [41]. It shows various applicability for more complex AM problems. For example, *Figure 15* lists the more complicated in-situ L-PBF images. Traditional method requests to design a special algorithm for each type of anomaly. For example, *Figure 15* (a), (b), and (f) requests the algorithm to use different greyscale and clustering methods to distinguish the melt pool and spatters. The outline of the melt pool in *Figure 15* (b), (c), (d) and (e) can be difficult to detect by simply counting the pixels. Future works would focus on more complex anomaly detection of L-PBF and build the connection between melt pool features and AM design process [42].

## VI. ACKNOWLEDGEMENTS

This material is based upon work supported by the National Institute of Standards and Technology (NIST) under Cooperative Agreement number NIST 70NANB18H258.

## VII. DISCLAIMER

Certain commercial systems are identified in this paper. Such identification does not imply recommendation or endorsement by NIST; nor does it imply that the products identified are necessarily the best available for the purpose. Further, any opinions, findings, conclusions, or recommendations expressed in this material are those of the authors and do not necessarily reflect the views of NIST or any other supporting U.S. government or corporate organizations.

## VIII. REFERENCES

[1] Frazier, W. E., 2014, "Metal Additive Manufacturing: A Review," *Journal of Materials Engineering and Performance*, **23**(6) pp. 1917-1928.  
 [2] King, W. E., Anderson, A. T., Ferencz, R., 2015, "Laser Powder Bed Fusion Additive Manufacturing of Metals; Physics, Computational, and Materials Challenges," *Applied Physics Reviews*, **2**(4) pp. 041304.

[3] Witherell, P., Feng, S., Simpson, T. W., 2014, "Toward Metamodels for Composable and Reusable Additive Manufacturing Process Models," *Journal of Manufacturing Science and Engineering*, **136**(6) pp. 061025.  
 [4] Liu, Y., Li, S., Wang, H., 2016, "Microstructure, Defects and Mechanical Behavior of Beta-Type Titanium Porous Structures Manufactured by Electron Beam Melting and Selective Laser Melting," *Acta Materialia*, **113**pp. 56-67.  
 [5] Cunningham, R., Narra, S. P., Montgomery, C., 2017, "Synchrotron-Based X-Ray Microtomography Characterization of the Effect of Processing Variables on Porosity Formation in Laser Power-Bed Additive Manufacturing of Ti-6Al-4V," *Jom*, **69**(3) pp. 479-484.  
 [6] Tang, M., Pistorius, P. C., and Beuth, J. L., 2017, "Prediction of Lack-of-Fusion Porosity for Powder Bed Fusion," *Additive Manufacturing*, **14**pp. 39-48.  
 [7] Liu, C., Tian, X., Tang, H., 2013, "Microstructural Characterization of Laser Melting Deposited Ti-5Al-5Mo-5V-1Cr-1Fe Near B Titanium Alloy," *Journal of Alloys and Compounds*, **572**pp. 17-24.  
 [8] Lu, Y., Yang, Z., Eddy, D., 2018, "Self-Improving Additive Manufacturing Knowledge Management," *ASME 2018 International Design Engineering Technical Conferences and Computers and Information in Engineering Conference*, Anonymous American Society of Mechanical Engineers, pp. V01BT02A016-V01BT02A016.  
 [9] Thijs, L., Verhaeghe, F., Craeghs, T., 2010, "A Study of the Microstructural Evolution during Selective Laser Melting of Ti-6Al-4V," *Acta Materialia*, **58**(9) pp. 3303-3312.  
 [10] Lopez, F., Witherell, P., and Lane, B., 2016, "Identifying Uncertainty in Laser Powder Bed Fusion Additive Manufacturing Models," *Journal of Mechanical Design*, **138**(11) pp. 114502.  
 [11] Hussein, A., Hao, L., Yan, C., 2013, "Finite Element Simulation of the Temperature and Stress Fields in Single Layers Built without-Support in Selective Laser Melting," *Materials & Design* (1980-2015), **52**pp. 638-647.  
 [12] Criales, L. E., Arisoy, Y. M., Lane, B., 2017, "Laser Powder Bed Fusion of Nickel Alloy 625: Experimental Investigations of Effects of Process Parameters on Melt Pool Size and Shape with Spatter Analysis," *International Journal of Machine Tools and Manufacture*, **121**pp. 22-36.  
 [13] Beal, V., Erasenthiran, P., Hopkinson, N., 2006, "The Effect of Scanning Strategy on Laser Fusion of Functionally Graded H13/Cu Materials," *The International Journal of Advanced Manufacturing Technology*, **30**(9-10) pp. 844-852.  
 [14] Grasso, M., and Colosimo, B. M., 2017, "Process Defects and in Situ Monitoring Methods in Metal Powder Bed Fusion: A Review," *Measurement Science and Technology*, **28**(4) pp. 044005.  
 [15] Craeghs, T., Clijsters, S., Kruth, J., 2012, "Detection of Process Failures in Layerwise Laser Melting with Optical Process Monitoring," *Physics Procedia*, **39**pp. 753-759.  
 [16] Price, S., Cooper, K., and Chou, K., 2012, "Evaluations of temperature measurements by near-infrared thermography in powder-based electron-beam additive manufacturing," *Proceedings of the Solid Freeform Fabrication Symposium*, Anonymous University of Texas, Austin, TX, pp. 761-773.  
 [17] Lott, P., Schleifenbaum, H., Meiners, W., 2011, "Design of an Optical System for the in Situ Process Monitoring of Selective Laser Melting (SLM)," *Physics Procedia*, **12**pp. 683-690.  
 [18] Santospirito, S., Słyk, K., Luo, B., 2013, "Detection of defects in laser powder deposition (LPD) components by pulsed laser transient thermography," *Thermosense: Thermal Infrared Applications XXXV*, Anonymous International Society for Optics and Photonics, **8705**, pp. 87050X.  
 [19] Gunenthiram, V., Peyre, P., Schneider, M., 2018, "Experimental Analysis of Spatter Generation and Melt-Pool

- Behavior during the Powder Bed Laser Beam Melting Process," *Journal of Materials Processing Technology*, **251**pp. 376-386.
- [20] Islam, M., Purtonen, T., Piili, H., 2013, "Temperature Profile and Imaging Analysis of Laser Additive Manufacturing of Stainless Steel," *Physics Procedia*, **41**pp. 835-842.
- [21] Yeung, H., Lane, B., Donmez, M., 2018, "Implementation of Advanced Laser Control Strategies for Powder Bed Fusion Systems," *Procedia Manufacturing*, **26**pp. 871-879.
- [22] Scime, L., and Beuth, J., 2018, "Anomaly Detection and Classification in a Laser Powder Bed Additive Manufacturing Process using a Trained Computer Vision Algorithm," *Additive Manufacturing*, **19**pp. 114-126.
- [23] DeCost, B. L., and Holm, E. A., 2017, "Characterizing Powder Materials using Keypoint-Based Computer Vision Methods," *Computational Materials Science*, **126**pp. 438-445.
- [24] Gobert, C., Reutzel, E. W., Petrich, J., 2018, "Application of Supervised Machine Learning for Defect Detection during Metallic Powder Bed Fusion Additive Manufacturing using High Resolution Imaging," *Additive Manufacturing*, **21**pp. 517-528.
- [25] Aminzadeh, M., and Kurfess, T. R., 2018, "Online Quality Inspection using Bayesian Classification in Powder-Bed Additive Manufacturing from High-Resolution Visual Camera Images," *Journal of Intelligent Manufacturing*, pp. 1-19.
- [26] Islam, M., Purtonen, T., Piili, H., 2013, "Temperature Profile and Imaging Analysis of Laser Additive Manufacturing of Stainless Steel," *Physics Procedia*, **41**pp. 835-842.
- [27] Furumoto, T., Alkahari, M. R., Ueda, T., 2012, "Monitoring of Laser Consolidation Process of Metal Powder with High Speed Video Camera," *Physics Procedia*, **39**pp. 760-766.
- [28] Dadbakhsh, S., Hao, L., and Sewell, N., 2012, "Effect of Selective Laser Melting Layout on the Quality of Stainless Steel Parts," *Rapid Prototyping Journal*, **18**(3) pp. 241-249.
- [29] Song, Y., and Koenig, W., 1997, "Experimental Study of the Basic Process Mechanism for Direct Selective Laser Sintering of Low-Melting Metallic Powder," *CIRP Annals*, **46**(1) pp. 127-130.
- [30] Krauss, H., Eschey, C., and Zaeh, M., 2012, "Thermography for monitoring the selective laser melting process," *Proceedings of the Solid Freeform Fabrication Symposium*, Anonymous pp. 999-1014.
- [31] Tapia, G., and Elwany, A., 2014, "A Review on Process Monitoring and Control in Metal-Based Additive Manufacturing," *Journal of Manufacturing Science and Engineering*, **136**(6) pp. 060801.
- [32] Lane, B., Mekhontsev, S., Grantham, S., 2016, "Design, developments, and results from the nist additive manufacturing metrology testbed (ammt)," *Solid Freeform Fabrication Symposium*, Austin, TX, Anonymous pp. 1145-1160.
- [33] Hooper, P. A., 2018, "Melt Pool Temperature and Cooling Rates in Laser Powder Bed Fusion," *Additive Manufacturing*, **22**pp. 548-559.
- [34] Khairallah, S. A., Anderson, A. T., Rubenchik, A., 2016, "Laser Powder-Bed Fusion Additive Manufacturing: Physics of Complex Melt Flow and Formation Mechanisms of Pores, Spatter, and Denudation Zones," *Acta Materialia*, **108**pp. 36-45.
- [35] Gander, W., Golub, G. H., and Strebler, R., "Least-Squares Fitting of Circles and Ellipses," .
- [36] LeCun, Y., Bottou, L., Bengio, Y., 1998, "Gradient-Based Learning Applied to Document Recognition," *Proceedings of the IEEE*, **86**(11) pp. 2278-2324.
- [37] Krizhevsky, A., Sutskever, I., and Hinton, G. E., 2012, "Imagenet classification with deep convolutional neural networks," *Advances in neural information processing systems*, Anonymous pp. 1097-1105.
- [38] Moges, T., Ameta, G., and Witherell, P., 2019, "A Review of Model Inaccuracy and Parameter Uncertainty in Laser Powder Bed Fusion Models and Simulations," *Journal of Manufacturing Science and Engineering*, **141**(4) pp. 040801.
- [39] Moges, T., Yan, W., Lin, S., 2018, "Quantifying Uncertainty in Laser Powder Bed Fusion Additive Manufacturing Models and Simulations," *Solid Freeform Fabrication Symposium An Additive Manufacturing Conference*.
- [40] Razvi, S. S., Feng, S., Narayanan, A., Lee, Y. T., and Witherell, P. "A Review of Machine Learning Applications in Additive Manufacturing." In *Proceedings of the ASME 2019 International Design Engineering Technical Conferences and Computers and Information in Engineering Conference*, 10. Anaheim, CA, USA: ASME, 2019.
- [41] H. Ko, P. Witherell, N. Y. Ndiaye and Y. Lu, "Machine Learning based Continuous Knowledge Engineering for Additive Manufacturing," *2019 IEEE 15th International Conference on Automation Science and Engineering (CASE)*, Vancouver, BC, Canada, 2019, Accepted.
- [42] Kim, S., Rosen, D.W., Witherell, P. and Ko, H., 2018, August. A Design for Additive Manufacturing Ontology to Support Manufacturability Analysis. In *ASME 2018 International Design Engineering Technical Conferences and Computers and Information in Engineering Conference* (pp. V02AT03A036-V02AT03A036). American Society of Mechanical Engineers.